

# Solution of the equation of radiative transfer using a Newton–Krylov approach and adaptive mesh refinement

Marc R.J. Charest\*, Clinton P.T. Groth, Ömer L. Gülder

University of Toronto, Institute for Aerospace Studies, 4925 Dufferin Street, Toronto, Ontario, Canada M3H 5T6

## ARTICLE INFO

### Article history:

Received 11 February 2010

Received in revised form 4 November 2011

Accepted 10 November 2011

Available online 25 November 2011

### Keywords:

Radiation transport

Discrete ordinates method

Finite-volume method

Parallel solution

Numerical modeling

Adaptive mesh refinement

## ABSTRACT

The discrete ordinates method (DOM) and finite-volume method (FVM) are used extensively to solve the radiative transfer equation (RTE) in furnaces and combusting mixtures due to their balance between numerical efficiency and accuracy. These methods produce a system of coupled partial differential equations which are typically solved using space-marching techniques since they converge rapidly for constant coefficient spatial discretization schemes and non-scattering media. However, space-marching methods lose their effectiveness when applied to scattering media because the intensities in different directions become tightly coupled. When these methods are used in combination with high-resolution limited total-variation-diminishing (TVD) schemes, the additional non-linearities introduced by the flux limiting process can result in excessive iterations for most cases or even convergence failure for scattering media. Space-marching techniques may also not be quite as well-suited for the solution of problems involving complex three-dimensional geometries and/or for use in highly-scalable parallel algorithms. A novel pseudo-time marching algorithm is therefore proposed herein to solve the DOM or FVM equations on multi-block body-fitted meshes using a highly scalable parallel-implicit solution approach in conjunction with high-resolution TVD spatial discretization. Adaptive mesh refinement (AMR) is also employed to properly capture disparate solution scales with a reduced number of grid points. The scheme is assessed in terms of discontinuity-capturing capabilities, spatial and angular solution accuracy, scalability, and serial performance through comparisons to other commonly employed solution techniques. The proposed algorithm is shown to possess excellent parallel scaling characteristics and can be readily applied to problems involving complex geometries. In particular, greater than 85% parallel efficiency is demonstrated for a strong scaling problem on up to 256 processors. Furthermore, a speedup of a factor of at least two was observed over a standard space-marching algorithm using a limited scheme for optically thick scattering media. Although the time-marching approach is approximately four times slower for absorbing media, it vastly outperforms standard solvers when parallel speedup is taken into account. The latter is particularly true for geometrically complex computational domains.

© 2011 Elsevier Inc. All rights reserved.

## 1. Introduction

Detailed treatment of radiation heat transfer is essential to the development of mathematical models that accurately describe combusting flows. Unfortunately, modelling radiative heat transfer can be an arduous task requiring the solution

\* Corresponding author.

E-mail address: [charest@utias.utoronto.ca](mailto:charest@utias.utoronto.ca) (M.R.J. Charest).

of complex integro-differential equations with many degrees of freedom and widely varying properties. Numerical solution is generally required as exact solutions exist only for idealized cases that do not realistically describe typical reactive flows. Since detailed combustion models must also incorporate complex chemistry, turbulence, and multi-species transport, the remaining computational resources available for radiation transport may be limited. As such, there is a need for accurate, scalable and efficient radiation solvers that can be fully coupled to today's computational fluid dynamics (CFD) solution algorithms and take advantage of growing trends towards large-scale parallel computing. This paper presents a new parallel-implicit framework for solving the radiative transfer equation (RTE) on adaptively-refined multi-block body-fitted mesh for the treatment of both emitting-absorbing and anisotropically scattering media on geometrically complex computational domains.

The spectral intensity, which characterizes the radiation field in non-gray participating media, varies with location in space, direction of photon or electromagnetic wave travel, and wavenumber. This large number of degrees of freedom coupled with the dependence of radiative properties on temperature, pressure, and composition makes solving the RTE a formidable task. Additional difficulties for numerical solution techniques are created by the tight coupling that arises between intensities in each direction for scattering media.

Two proven effective numerical techniques for solving the RTE are the discrete ordinates method (DOM) [1] and finite-volume method (FVM) [2,3]. Both techniques discretize the solid angle describing the direction of propagation to create a set of partial differential equations (PDEs) with only spatial coordinates as independent variables. As a result, standard finite-difference or finite-volume spatial discretization techniques that are commonly used in CFD can be applied. The two methods differ only by the angular discretization technique. In the DOM, the RTE is solved for specific ordinate directions and integrals over the solid angle are evaluated as weighted summations using numerical quadrature. Ordinate directions and weights are somewhat arbitrary, but they are usually derived using moment matching techniques [4] or geometric principles [5]. The importance of matching full-range moments of intensity on source terms in the RTE and first moments over the half-range on boundary conditions are discussed by both Fiveland [6] and Truelove [7]. This inability to exactly match all half- and full-range moments leads to problems with the conservation of energy and is the main drawback to this method. To overcome this, the FVM discretizes the solid angle into control-angle elements and the RTE is solved for the average intensity in each control-angle. Integrals over the solid angle may then be evaluated using "exact" integration to the order of the discretization scheme. For Cartesian meshes where the edges of the control-angle elements are aligned with the grid lines, the method is fully conservative as all full-range moments are satisfied. The FVM may also be applied to irregular geometry in a fully conservative manner provided that control-angle overlap is properly addressed [8].

The DOM and FVM both suffer from several drawbacks, the most significant are errors due to false scattering or numerical diffusion and those due to angular discretization. In the DOM, angular discretization errors, or ray effects, can result from approximating the continuously varying intensity with discrete directions and are independent of spatial differencing practices [9]. Ray concentration errors arise in the FVM when a piecewise-constant approximation is made but the intensity is not uniform within each control angle [8]. As a result of this approximation, any concentrated beams originating from a point are smeared over the whole control angle. Despite these errors, the FVM shows promise since higher-order representations for the variance of the spectral intensity with solid angle may be employed to reduce ray concentration errors without overly fine angular discretizations. However, extension of existing FVM formulations to high-order angular and spatial discretizations is not completely obvious.

Due to the linear upwind nature of the RTE, space-marching techniques are commonly applied to solve both the DOM and FVM equations. For a particular direction or control-angle element, the solution in each cell is computed starting at the upwind-most corner where boundary values can be specified. The solution in the neighboring downstream cells are then determined by sequentially marching in the direction of interest. This procedure is carried out until the entire solution domain is swept in each direction. For non-scattering media, non-reflecting boundaries and constant coefficient spatial discretization schemes, a converged solution can be obtained in one full sweep of the domain as the intensity at the downstream boundaries is related directly to upstream quantities. However, constant coefficient schemes are either overly dissipative or unstable as only first-order upwind schemes guarantee positivity [10]. Liu et al. [10] and Jessee and Fiveland [11] have applied bounded high-resolution schemes developed for CFD to the DOM. The schemes considered include the SMART [12], MUSCL [13], CLAM [14], and minmod [15] which avoid spurious oscillations near discontinuities that would otherwise occur with high-order spatial discretizations by limiting. Both investigators were able to achieve bounded solutions with a dramatic increase in accuracy at the expense of computational efficiency. Coelho [16] reformulated the SMART, MUSCL, and CLAM schemes such that interpolation was performed in the ordinate directions. These skew high-order schemes yielded further improvements in accuracy yet required more iterations than their non-skew counterparts. It is obvious that there exists a need for improved solution techniques that readily handle the local non-linearities introduced by high-resolution schemes without significant increase in solution time.

Standard space-marching algorithms exhibit significant performance degradation when applied to scattering media with high optical thickness where strong coupling exists between the intensities in different directions. Such computations can require a large number of iterations to converge, are prone to unphysical oscillations, and/or can even fail to converge. While standard techniques for solving linear equations may be used to cope with this coupling, large storage requirements can be prohibitive even for coarse angular and spatial discretizations. Many researchers have developed algorithms to accelerate the convergence of standard space-marching techniques (see [17] and references therein). One popular technique is diffusion synthetic acceleration (DSA) [18,19]. This method first applies a source iteration or transport sweep and then solves a

lower-order diffusion approximation to correct the flux for in-scattering effects. While DSA is effective for a wide variety of problems involving scattering, it can break down in multi-dimensional problems with optically thick computational cells, discontinuities in medium properties or large scattering cross sections [20]. The method also requires the solution of an additional linear system for the discretized diffusion approximation which can be costly in multiple dimensions [20]. Warsa et al. [20] successfully improved convergence in cases where the standard DSA algorithm failed by applying a Krylov iterative space-marching technique [21] preconditioned with the DSA. However, their algorithm does not fully couple the equations for each direction and does not address local non-linearities introduced by high-resolution schemes. Mathur and Murthy [22] have devised a point-implicit coupled solution procedure that accelerates convergence in optically-thick scattering media by updating the intensities in all directions for a particular cell simultaneously. The procedure was most effective for moderate to high optical thicknesses and relatively simple scattering phase functions. Multigrid methods have also been used to help accelerate the solution of the RTE in conjunction with either space-marching or other relaxation techniques [17,23]. However, spatial multigrid alone is ineffective in accelerating the convergence of space-marching algorithms applied to optically-thick, highly-scattering media [23].

Several researchers have begun applying time-evolution solution techniques to cope with arbitrary meshes and scattering media. Fiterman et al. [24] developed a finite-volume pseudo-time stepping solution procedure specifically for the DOM. They employed an explicit Euler temporal discretization with multigrid acceleration and an artificial viscosity-based spatial discretization. Selçuk and co-workers [25–27] have applied the method of lines (MOL) to solve the DOM equations in a variety of applications. A three-dimensional DOM solver based on the MOL was presented by Selçuk and Kirbaş [25] and applied to a rectangular enclosure with black walls, a gray absorbing-emitting medium, and steep temperature gradients. Spatial gradients were evaluated using linear upwind and biased-upwind finite-differences and the equations were relaxed to a steady-state using both the LSODE [28] and RKF45 [29] ordinary differential equation (ODE) solvers. Ayranci and Selçuk [26] later compared these differencing procedures with more advanced second-order upwind total-variation-diminishing (TVD) schemes using the Van Leer and Superbee limiter functions on uniform grids. Third- and fifth-order biased WENO [30] and MPWENO [31] finite-difference schemes were also assessed by the authors. They found that the Van Leer limiter provided the best results based on accuracy and efficiency when coupled with the RKF45 solver. In general, high-order schemes were found to have stability problems and require extremely small time-step sizes for stable integration.

To avoid these issues, McClarren et al. [32,33] developed a quasi-linear TVD solution procedure based on the minmod [15] slope limiter. The procedure first solves the problem using a first-order upwind discretization to determine the direction of interpolation. A second linear system is solved to determine the final second-order solution. However, this exploit is only possible using the minmod [15] limiter which is overly-dissipative when applied to multi-dimensional irregular mesh [34]. The resulting solution is also not guaranteed to strictly satisfy the TVD condition.

Others have looked at the use of implicit time-marching methods in conjunction with high-resolution discretizations, since these methods offer improved stability and convergence characteristics. Balsara [35] solved the DOM for emitting-absorbing and scattering media using a multi-dimensional fluctuation-splitting scheme [36,37]. In Balsara's work, the discretized equations were relaxed to a steady-state with full-approximation storage (FAS) multigrid [38] and a restarted Newton-Krylov method [39] as a nonlinear smoother. While good convergence properties were observed in both optically thick and thin media, the performance and memory requirements compared to standard space-marching techniques were not discussed. The large amount of memory required for the implicit smoother on each multigrid level would probably prohibit the application of this approach to large-scale CFD problems. Another implicit approach is that of Chai [40], who solved the transient FVM equations for radiative transfer with scattering media in irregular geometries. This approach made use of a tri-diagonal matrix solver and the CLAM scheme. Neither of these two implicit approaches discussed here is directly compatible with standard parallel solution techniques.

Aside from the challenges associated with the treatment of complex geometries and scattering media, parallel implementations of conventional space-marching techniques can also be problematic and/or very challenging, particularly for complex grid topologies. Gonçalves and Coelho [41,42] have studied parallel space-marching implementations of the DOM and FVM using both angular and spatial decomposition strategies. The authors found that while angular decomposition strategies yielded high efficiencies and speedups, their scalability is limited by the size of the angular discretization which is typically much coarser than the spatial discretization. Additionally, these methods require excessive communication when evaluating integrals over the solid angle and do not readily integrate with commonly used parallel CFD solution techniques based on domain decomposition. Gonçalves and Coelho's work also showed that domain decomposition strategies applied to standard space-marching solvers yield only modest parallel efficiencies despite their attempt to devise an optimized sweeping procedure. In other work, Baker and Koch [43] developed a parallel sweep procedure for structured mesh that effectively scaled up to 2048 processors. The method used a special columnar domain decomposition and sweep ordering algorithm to obtain high parallel efficiencies. However, this ordering method breaks down for three-dimensional unstructured mesh as cyclic dependencies between cells develop. By adding a pipelining strategy and prioritization heuristics, Pautz [44] successfully extended this algorithm to unstructured mesh. Parallel efficiencies of approximately 60% were achieved on 128 processors. These type of ordered sweep parallel strategies have also been applied in conjunction with adaptive mesh refinement (AMR) and synthetic acceleration algorithms for structured [45,46] and unstructured [47] mesh.

Other parallel strategies for solution of the RTE have also been considered. Liu et al. [48] developed a spatial-domain-based parallel algorithm for the FVM, solving the equations semi-implicitly with a conjugate gradients method and Dupont-Kendall-Rachford incomplete factorization. Modest performance was achieved on up to 18 processors. An AMR

algorithm with a similar parallel sweeping strategy as the one proposed by Gonçalves and Coelho [41,42] was developed by Howell [49]. Krishnamoorthy et al. [50] applied several iterative matrix solvers to a spatially decomposed DOM but sequentially solved the intensity for each direction. Using both block and point Jacobi preconditioners, the parallel performance deteriorated when more than 8 processors were employed. Yıldız and Bedir [51] applied a pipeline parallelization strategy to improve processor utilization over standard parallel sweeping algorithms. Parallel efficiencies of 70% were observed with 20 processors.

Of particular importance to this work is the parallel framework for solving transient reacting laminar diffusion flames proposed by Bilge et al. [27]. Their framework uses domain decomposition combined with the same MOL scheme for the DOM developed by Selçuk and co-workers that was previously mentioned. The work clearly illustrates the rather straightforward applicability of spatial decomposition and time-marching methods to the parallel solution of the RTE.

In the present study, a cell-centred, flux-based, upwind finite-volume discretization procedure is applied on multi-block body-fitted quadrilateral meshes to solve the PDEs resulting from the DOM and FVM. Multiple solution scales associated with optically thin and thick media are accurately resolved using the block-based AMR algorithm described by Sachdev et al. [52,53]. The algorithm uses a flexible block-based hierarchical data structure to facilitate automatic solution-directed mesh adaptation according to physics-based refinement criteria. It is applicable to general multi-block body-fitted anisotropic (stretched) mesh with arbitrary quadrilateral cells. While AMR has been applied to the solution of radiation transport using finite-volume [45–47] and finite element [54–57] discretizations, the previous research is not applicable to these types of mesh. For example, the block-based AMR algorithm developed by Baker et al. [45,46], which is the most relevant to the present research, is applicable for Cartesian mesh only. The algorithm developed and used here is far more general and suitable for mesh blocks with different resolutions and anisotropic (stretched) quadrilateral cells. This allows for the treatment of more complex geometries without the use of the cut cell or overlapping grid approaches generally adopted in Cartesian mesh methods.

To cope with non-linearities introduced by the spatial discretization and equation coupling, the parallel implicit time-evolution/relaxation procedure of Groth and Northrup [58] is employed. This relaxation algorithm uses a matrix-free inexact Newton method and the generalized minimal residual method (GMRES) [59] to solve the resulting non-symmetric system of linear equations at each step of the Newton algorithm. Right preconditioning of the linear system in conjunction with an additive Schwarz global preconditioner is applied. The block-based data structure and Schwarz preconditioning naturally lend themselves to domain decomposition and thereby enable efficient and scalable implementations of the algorithm on modern distributed-memory multiprocessor architectures. The proposed solution algorithm for the RTE is highly scalable with high parallel efficiency and is well suited for the treatment of problems involving complex geometry and scattering media. In the following sections, the numerical procedure is discussed in detail and applied to several test cases. A discussion of the results and suggestions for future research conclude the paper.

## 2. Numerical method

The RTE for a monochromatic beam of light in the direction  $\hat{\mathbf{s}}$  is given by

$$\frac{1}{c} \frac{\partial I}{\partial t} + \frac{\partial I}{\partial s} = \frac{1}{c} \frac{\partial I}{\partial t} + \hat{\mathbf{s}} \cdot \nabla I = \kappa I_b - (\kappa + \sigma_s) I + \frac{\sigma_s}{4\pi} \int_{4\pi} I(\hat{\mathbf{s}}') \Phi(\hat{\mathbf{s}}', \hat{\mathbf{s}}) d\Omega' \quad (1)$$

where  $c$  is the speed of light in a vacuum,  $I$  is the intensity in the direction of  $\hat{\mathbf{s}}$ ,  $I_b$  is the blackbody radiative intensity,  $\kappa$  and  $\sigma_s$  are the absorption and scattering coefficients,  $\Phi(\hat{\mathbf{s}}', \hat{\mathbf{s}})$  is the scattering phase function, and  $\Omega$  is the solid angle. The phase function describes the probability that a ray traveling in direction  $\hat{\mathbf{s}}'$  will be scattered into the direction  $\hat{\mathbf{s}}$ . Eq. (1) is a first-order linear integro-differential equation with five independent variables;  $I$  is a function of three position variables ( $x, y, z$ ) and two angular variables ( $\theta, \psi$ ) which define the solid angle  $\Omega$ . Here,  $\theta$  and  $\psi$  are the polar and azimuthal angles, respectively, as illustrated in Fig. 1. The direction cosine vector,  $\hat{\mathbf{s}}$ , is related to  $\theta$  and  $\psi$  by

$$\hat{\mathbf{s}} = \mu \hat{\mathbf{i}} + \eta \hat{\mathbf{j}} + \zeta \hat{\mathbf{k}} = (\sin \theta \cos \psi) \hat{\mathbf{i}} + (\sin \theta \sin \psi) \hat{\mathbf{j}} + (\cos \theta) \hat{\mathbf{k}} \quad (2)$$

where  $\hat{\mathbf{i}}$ ,  $\hat{\mathbf{j}}$ , and  $\hat{\mathbf{k}}$  are the unit normal vectors aligned with the  $x$ ,  $y$ , and  $z$  axes, respectively.

Due to the complex nature of the RTE, few exact solutions exist even for relatively simple problems [60,61] and its solution must therefore be obtained numerically. Of the many different solution techniques developed to accommodate the angular nature of radiative heat transfer (see Viskanta and Mengüç [62] for a review of solution techniques), the DOM and FVM are considered in this work. Both of these schemes reduce the number of independent variables by discretizing the angular dependence of intensity and produce a set of PDEs with only spatial and temporal gradients. These PDEs are linear hyperbolic and thus many of the techniques developed for solving the Euler equations of compressible gas dynamics can be applied. Since the two techniques differ only slightly from each other, a general formulation applicable for both will be derived.

Applying the DOM to the RTE yields

$$\frac{1}{c} \frac{\partial I_m}{\partial t} + \hat{\mathbf{s}}_m \cdot \nabla I_m = \kappa I_b - (\kappa + \sigma_s) I_m + \frac{\sigma_s}{4\pi} \sum_{n=1}^M w_n I_n \Phi(\hat{\mathbf{s}}_n, \hat{\mathbf{s}}_m) \quad (3)$$

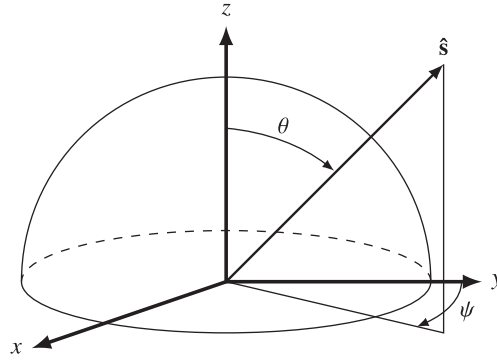


Fig. 1. Solid angle and coordinate system.

where the subscript,  $m$ , denotes the discrete ordinate direction,  $M$  is the total number of ordinate directions,  $I_m$  is the intensity in the  $m$ th direction, and  $\mathbf{s}_m$  and  $w_m$  are the ordinate direction vector and associated quadrature weight. The FVM equations are obtained by discretizing the solid angle into  $M$  control-angle elements and integrating the RTE over each element to give

$$\frac{1}{c} \frac{\partial I_m}{\partial t} + \mathbf{s}_m \cdot \nabla I_m = \kappa I_b - (\kappa + \sigma_s) I_m + \frac{\sigma_s}{4\pi} \sum_{n=1}^M I_n \Phi_{mn} \Delta\Omega_n \tag{4}$$

where the control-angle-averaged direction cosine vector,  $\mathbf{s}_m$ , and phase function,  $\Phi_{mn}$ , are defined as

$$\Phi_{mn} = \frac{1}{\Delta\Omega_m \Delta\Omega_n} \int_{\Delta\Omega_m} \int_{\Delta\Omega_n} \Phi(\hat{\mathbf{s}}', \hat{\mathbf{s}}) d\Omega' d\Omega \tag{5}$$

$$\mathbf{s}_m = \frac{1}{\Delta\Omega_m} \int_{\Delta\Omega_m} \hat{\mathbf{s}} d\Omega \tag{6}$$

Eq. (4) was derived assuming piecewise-constant intensity over each control angle and therefore  $I_m$  represents the average intensity in  $m$ th control angle. This first-order approximation limits the overall order of the solution regardless of spatial (or temporal for transient analyses) discretization practices. This accuracy limitation will be addressed further in the following sections.

Let us now consider a two-dimensional Cartesian coordinate system. The proposed algorithm extends readily to three-dimensions but such extensions are not the focus here. Both Eqs. (3) and (4) can be reformulated into a weak-conservation form since  $\hat{\mathbf{s}}_m$  and  $\mathbf{s}_m$  are independent of spatial location. The resulting equation is given by

$$\frac{\partial I_m}{\partial t} + \frac{\partial}{\partial x}(c\mu_m I_m) + \frac{\partial}{\partial y}(c\eta_m I_m) = S_m \tag{7}$$

where the source term  $S_m$  is defined as the right-hand side (RHS) of either Eq. (3) or (4) for the DOM or FVM, respectively, multiplied by the speed of light ( $c$ ). The directional coefficients  $\mu_m$  and  $\eta_m$  are either the direction cosines defined by the numerical quadrature scheme or the  $x$  and  $y$  components of  $\mathbf{s}_m$ . Eq. (7) can be re-expressed in vector form as

$$\frac{\partial \mathbf{U}}{\partial t} + \frac{\partial \mathbf{F}}{\partial x} + \frac{\partial \mathbf{G}}{\partial y} = \mathbf{S} \tag{8}$$

where the solution vector,  $\mathbf{U}$ ,  $x$ -direction flux,  $\mathbf{F}$ ,  $y$ -direction flux,  $\mathbf{G}$ , and source vector,  $\mathbf{S}$ , are defined by

$$\left. \begin{aligned} \mathbf{U} &= I_m \\ \mathbf{F} &= c\mu_m I_m \\ \mathbf{G} &= c\eta_m I_m \\ \mathbf{S} &= S_m \end{aligned} \right\} \text{ for } m = 1, \dots, M \tag{9}$$

### 2.1. Finite-volume spatial discretization scheme

The proposed scheme for the RTE uses an upwind finite-volume spatial discretization procedure in conjunction with limited linear solution reconstruction to solve Eq. (8). It is applied on a multi-block mesh composed of arbitrary quadrilateral cells, which is illustrated in Fig. 2. Integrating Eq. (8) over a control volume yields

$$\frac{d}{dt} \int_A \mathbf{U} dA + \oint_{\Gamma} \bar{\mathbf{F}}(\mathbf{U}) \cdot \hat{\mathbf{n}} dl = \int_A \mathbf{S}(\mathbf{U}) dA \tag{10}$$

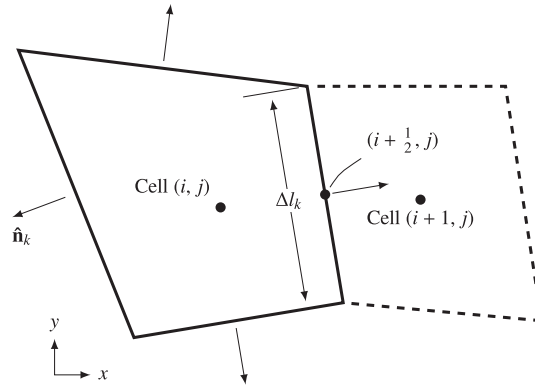


Fig. 2. Two-dimensional quadrilateral computational cell.

where  $A$  is the area of the computational cell,  $\vec{\mathbf{F}}(\mathbf{U}) = (\mathbf{F}, \mathbf{G})$  is the flux dyad,  $\hat{\mathbf{n}}$  and  $l$  are the face normal and length of the cell edge which lies on the surface contour defined by  $\Gamma$ . The cell-average solution state is defined as

$$\bar{\mathbf{U}} = \frac{1}{A} \int_A \mathbf{U} \, dA \quad (11)$$

Substituting this relation into Eq. (10), and applying the integration procedure to cell  $(i, j)$  results in a system of coupled semi-discrete ODEs given by

$$\frac{\partial \bar{\mathbf{U}}_{ij}}{\partial t} = -\frac{1}{A_{ij}} \sum_k (\vec{\mathbf{F}}_k \cdot \hat{\mathbf{n}}_k \Delta l_k)_{ij} + \mathbf{S}(\bar{\mathbf{U}}_{ij}) = \mathbf{R}_{ij}(\mathbf{U}) \quad (12)$$

where  $\Delta l_k$  is the length of face  $k$  and  $\mathbf{R}_{ij}$  is the residual vector. For Eq. (12), it has been assumed that

$$\frac{1}{A} \int_A \mathbf{S}(\mathbf{U}) \, dA \approx \mathbf{S}(\bar{\mathbf{U}}) \quad (13)$$

To determine the numerical flux at the cell face, a high-order upwind Godunov scheme is used. Godunov's method [63] begins by assuming that the solution in each cell is piecewise-constant and that the intermediate solution state at the cell interface is approximated by upwinding. It is this upwinding that ensures monotonicity and prevents any unwanted solution discontinuities. In two-dimensions, given the left and right solution states,  $\mathbf{U}_L$  and  $\mathbf{U}_R$ , the numerical flux at the cell interface is

$$\vec{\mathbf{F}} \cdot \hat{\mathbf{n}} = \mathcal{F}(\mathbf{U}_L, \mathbf{U}_R, \hat{\mathbf{n}}) \quad (14)$$

where  $\mathcal{F}$  is the upwind solution flux in a direction aligned along the face normal  $\hat{\mathbf{n}}$ .

The extension of Godunov's scheme to second-order can prove challenging as second-order schemes always generate oscillations [64]. Godunov's scheme is first-order accurate because the projection of the cell-averaged solution in each cell occurs on piecewise constant states. This projection is completely decoupled from the upwinding process and thus one can easily modify the spatial approximation. For this work, second-order spatial accuracy is achieved by interpolating the solution state at the cell face between the two neighboring cells. Monotonicity is ensured using limiters to control gradients locally and damp any over- and under-shoots [13]. The reconstructed left and right states for interface  $(i + \frac{1}{2}, j)$  in two-dimensions are

$$\mathbf{U}_L = \bar{\mathbf{U}}_{ij} + \phi_{ij} \left[ \frac{\partial \mathbf{U}}{\partial x} \Big|_{ij} (x_{i+\frac{1}{2}j} - x_{ij}) + \frac{\partial \mathbf{U}}{\partial y} \Big|_{ij} (y_{i+\frac{1}{2}j} - y_{ij}) \right] \quad (15)$$

$$\mathbf{U}_R = \bar{\mathbf{U}}_{i+1j} + \phi_{i+1j} \left[ \frac{\partial \mathbf{U}}{\partial x} \Big|_{i+1j} (x_{i+\frac{1}{2}j} - x_{i+1j}) + \frac{\partial \mathbf{U}}{\partial y} \Big|_{i+1j} (y_{i+\frac{1}{2}j} - y_{i+1j}) \right] \quad (16)$$

where  $\phi$  is the slope limiter. The linear least-squares reconstruction error minimization technique of Barth and Fredrickson [65] is used to evaluate the cell solution gradients. Slope limiting is performed with a slope limiter specifically designed for use in multiple dimensions [66].

## 2.2. Inexact Newton method

For cases involving scattering, the equations for radiative transport in each direction (Eq. (7)) become coupled through the source terms and this coupling increases with optical thickness. This angular coupling combined with the non-linearities introduced by the TVD spatial discretization scheme can be problematic for space-marching techniques. In many cases, these

solution techniques may require excessive iterations or even fail to converge. Newton's method is a robust and efficient non-linear solution technique and is applied in this work to overcome these difficulties. It is used to relax the semi-discrete form of the governing equations to steady-state such that

$$\mathbf{R}(\mathbf{U}) = \frac{d\bar{\mathbf{U}}}{dt} = \mathbf{0} \quad (17)$$

This particular implementation follows the algorithm developed previously by Groth and Northrup [58] specifically for use on large multi-processor parallel clusters. The implementation makes use of a Jacobian-free inexact Newton method coupled with an iterative Krylov subspace linear solver. In Newton's method, a solution to Eq. (17) is sought by iteratively solving a sequence of linear systems given an initial estimate,  $\mathbf{U}^0$ . Successively improved estimates are obtained by solving

$$\left(\frac{\partial \mathbf{R}}{\partial \mathbf{U}}\right)^n \Delta \mathbf{U}^n = \mathbf{J}(\mathbf{U}^n) \Delta \mathbf{U}^n = -\mathbf{R}(\mathbf{U}^n) \quad (18)$$

where  $\mathbf{J} = \frac{\partial \mathbf{R}}{\partial \mathbf{U}}$  is the residual Jacobian. The improved solution at step  $n$  is then determined from

$$\mathbf{U}^{n+1} = \mathbf{U}^n + \Delta \mathbf{U}^n \quad (19)$$

The Newton iterations proceed until some desired reduction of the norm of the residual is achieved and the condition  $\|\mathbf{R}(\mathbf{U}^n)\| < \epsilon \|\mathbf{R}(\mathbf{U}^0)\|$  is met. The tolerance,  $\epsilon$ , used in this work was  $10^{-10}$ .

For a system of nonlinear equations, each step of Newton's method requires the solution of the linear problem

$$\mathbf{J}\mathbf{x} = \mathbf{b} \quad (20)$$

where  $\mathbf{x} = \Delta \mathbf{U}$  and  $\mathbf{b} = -\mathbf{R}(\mathbf{U})$ . This system tends to be relatively large, sparse, and non-symmetric for which iterative methods have proven much more effective than direct methods. One effective method for a large variety of problems which is used here is the generalized minimal residual (GMRES) technique of Saad and co-workers [39,59,67,68]. This is an Arnoldi-based solution technique which generates orthogonal bases of the Krylov subspace to construct the solution. The technique is particularly attractive because the matrix  $\mathbf{J}$  is not explicitly formed and instead only matrix-vector products are required at each iteration to create new trial vectors. This drastically reduces the required storage. Another advantage is that iterations are terminated based on only a by-product estimate of the residual which does not require explicit construction of the intermediate residual vectors or solutions. Termination also generally only requires solving the linear system to some specified tolerance,  $\|\mathbf{R}^n + \mathbf{J}^n \Delta \mathbf{U}^n\|_2 < \zeta \|\mathbf{R}(\mathbf{U}^n)\|_2$ , where  $\zeta$  is typically in the range 0.1 – 0.5 [69]. We use a restarted version of the GMRES algorithm here, GMRES( $m$ ), that minimizes storage by restarting every  $m$  iterations.

Right preconditioning of  $\mathbf{J}$  is performed to help facilitate the solution of Eq. (20) without affecting the solution residual,  $\mathbf{b}$ . The preconditioning takes the form

$$(\mathbf{J}\mathbf{M}^{-1})(\mathbf{M}\mathbf{x}) = \mathbf{b} \quad (21)$$

where  $\mathbf{M}$  is the preconditioning matrix. A combination of an additive Schwarz global preconditioner and a block incomplete lower-upper (BILU) local preconditioner is used which is easily implemented in the block-based AMR scheme. In additive Schwarz preconditioning, the solution in each block is updated simultaneously and shared boundary data is not updated until a full cycle of updates has been performed on all domains. The preconditioner is defined as follows

$$\mathbf{M}^{-1} = \sum_{k=1}^{N_b} \mathbf{B}_k^T \mathbf{M}_k^{-1} \mathbf{B}_k \quad (22)$$

where  $N_b$  is the number of blocks and  $\mathbf{B}_k$  is the gather matrix for the  $k$ th domain. The local preconditioner,  $\mathbf{M}_k^{-1}$ , in Eq. (22) is based on block ILU( $p$ ) factorization [68] of the Jacobian for the first order approximation of each domain. The level of fill,  $p$ , was maintained at zero in order to minimize storage requirements. Larger values of  $p$  typically offer improved convergence characteristics for the linear system at the expense of storage.

### 2.3. Parallel adaptive mesh refinement scheme

Modelling practical combustion devices with complex chemistry, turbulence and radiation transport can quickly tax available computational resources even on relatively coarse meshes. Unfortunately, high mesh densities are required in areas with steep gradients and small length scales to accurately capture these processes. These locations can change over time and would normally require the use of large, fine uniform meshes. A flexible block-based AMR scheme is adopted here to limit the number of necessary computational cells by dynamically adapting the mesh to meet solution requirements. Details of the scheme and its implementation in parallel are described by Sachdev et al. [52,53]. The extension of the scheme to three dimensions is described by Gao and Groth [70]. In the proposed parallel implementation, block-based domain decomposition is applied to a body-fitted quadrilateral mesh. The resulting grid blocks are organized in a hierarchical quad-tree data structure to facilitate automatic solution-directed mesh adaptation with physics-based criteria. The scheme borrows aspects from previous work by Berger and co-workers [71–74], Quirk [75], and De Zeeuw and Powell [76] for Cartesian grids and has similarities with the block-based approaches described by Quirk and Hanebutte [77] and Berger and Saltzman [73].

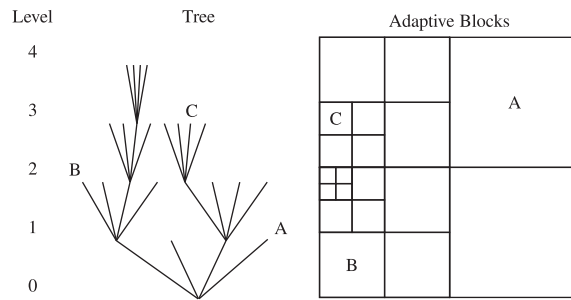


Fig. 3. Adaptive mesh refinement quad-tree data structure and associated solution blocks for a quadrilateral mesh.

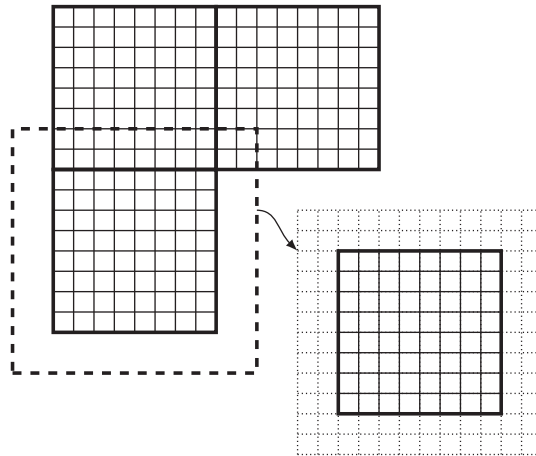


Fig. 4. Sample solution block with ghost cells.

The solution of Eq. (12) with AMR proceeds as follows. The equations are first integrated forward in time on an initial structured, multi-block mesh to obtain updated volume-averaged solution quantities. The mesh is then adapted by coarsening or refining the blocks designated by the refinement criteria. A hierarchical tree-like data structure, shown in Fig. 3, is used to retain connectivity between solution blocks and track their refinement history. The blocks requiring refinement are termed “parents” and are divided into four new blocks called “children”. Each child is a new block with the same number of cells as its parent, doubling the mesh resolution in the region. Coarsening flagged blocks is carried out by reversing this process and combining four children into one single parent.

To decrease the overall computational time, integration of the governing equations is performed in parallel. This is carried out by distributing the computational blocks among the available processors and simultaneously computing the solutions for each block on each processor. An even distribution of solution blocks is generally sought on homogeneous architectures while a weighted distribution is permissible for computations performed on heterogeneous systems such as networked workstations or computational grids. To ensure efficient load balancing, blocks are organized using a Morton ordering space filling curve which co-locates nearest neighbors on the same processor [74]. This minimizes the amount of necessary communication and improves the overall parallel efficiency of the implementation. The proposed AMR scheme was implemented using the message passing interface (MPI) library and the C++ programming language [78].

As shown in Fig. 4, ghost cells which surround the solution block and overlap cells on neighboring blocks are used to share solution content through inter-block communication. The conservation principle of the solution scheme is retained across blocks with resolution changes by using the fine-grid interface flux to correct the flux computed on neighboring coarse blocks [71,72]. Passing these flux corrections and the overlapping cell solutions between processors at each stage of the integration scheme accounts for the main source of inter-block communication.

### 3. Numerical results

A variety of test cases were examined as part of this study to analyze the performance of the algorithm in terms of discontinuity-capturing ability, spatial and angular accuracy, adaptive mesh refinement, parallel efficiency, and serial performance

compared to other standard solution algorithms. All computations were performed on a high performance parallel cluster consisting of 104 IBM P6-575 nodes with 128 GB RAM per node and a high-speed interconnect. The nodes each have 32 IBM POWER6 cores (4.7 GHz) and are connected to a non-blocking switch with four 4x-DDR InfiniBand links.

### 3.1. Transparent medium

The first test problem considered was a two-dimensional unit square enclosure defined on  $-0.5 \leq x \leq 0.5$  and  $-0.5 \leq y \leq 0.5$  with a transparent medium. For this case, all walls are black and cold ( $I_{bw} = 0$ ) except the bottom wall where  $I_{bw} = 1$ . This case is similar to the one previously studied by Coelho [16,79] who employed a variety of high-resolution schemes and compared the resulting solution errors. The problem is re-considered here only to verify that the current implementation properly captures solution discontinuities. In this test case, radiation propagating along a single direction with direction cosines corresponding to  $\mu = \eta = \sqrt{2}/2$  is computed. Numerical diffusion is expected to be large in this direction since the propagating ray makes a 45° angle with both the vertical and horizontal cell boundaries. The domain is discretized into 61 by 61 uniform cells and the solution computed using various schemes. The discretization schemes tested include the first-order upwind and second-order unlimited approximations, and the TVD schemes of Venkatakrisnan [80], Barth and Jespersen [81], Van Albada et al. [82], and Van Leer [14]. The computed intensity along the  $y$ -direction at  $x = 0$  is compared with the exact solution in Fig. 5. As expected, the upwind scheme is overly dissipative while unphysical oscillations are obtained using the second-order unlimited scheme. Limiting the second-order solution offers considerable improvement, with the Venkatakrisnan and Barth–Jespersen limiters outperforming the Van Albada and Van Leer limiters. The latter two limiters yield much smoother solutions which can be expected since they were primarily designed for one-dimension. The limiter of Venkatakrisnan was selected for all remaining test cases for its superior performance characteristics.

### 3.2. Discretization accuracy

The proposed scheme was analyzed in terms of spatial and angular accuracy through comparison with exact solutions for the RTE in rectangular enclosures. Similar to the previous test case, the enclosure for this study was taken to consist of a unit square except with all walls cold and black and containing a hot, absorbing-emitting medium with  $\kappa = 10 \text{ m}^{-1}$ . Exact solutions were previously derived by Cheng [60] for this particular problem. The overall error between numerical and exact solutions was defined by the change in the two-norm of the error in direction-integrated radiative intensity. It is defined as

$$\|\text{Error}\|_2 = \left\{ \frac{\sum_{i=1}^{N_c} [G_{\text{exact}}(x_i, y_i) - G_i]^2 A_i}{\sum_{i=1}^{N_c} A_i} \right\}^{1/2} \tag{23}$$

where  $N_c$  is the total number of cells,  $A_i$  is the cell area,  $G_{\text{exact}}(x_i, y_i)$  and  $G_i$  are the exact and numerical solution for the direction-integrated intensity evaluated at the center of the  $i$ th cell. The direction-integrated intensity is given by

$$G = \int_{4\pi} I(\hat{\mathbf{s}}) \, d\Omega \approx \sum_{m=1}^M \delta\Omega_m I_m \tag{24}$$

where  $\delta\Omega_m = w_m$  for the DOM and  $\delta\Omega_m = \Delta\Omega_m$  for the FVM, respectively.

The change in error between numerical and exact solutions of the RTE with increasing number of directions of propagation is illustrated in Fig. 6(a). Here, solutions were obtained on a fixed spatial grid of 64 by 64 uniform cells with either the

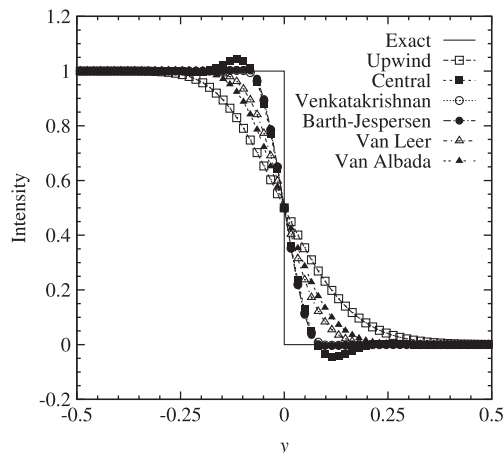


Fig. 5. Radiation intensity profiles along the vertical symmetry plane of a two-dimensional square enclosure with transparent medium.

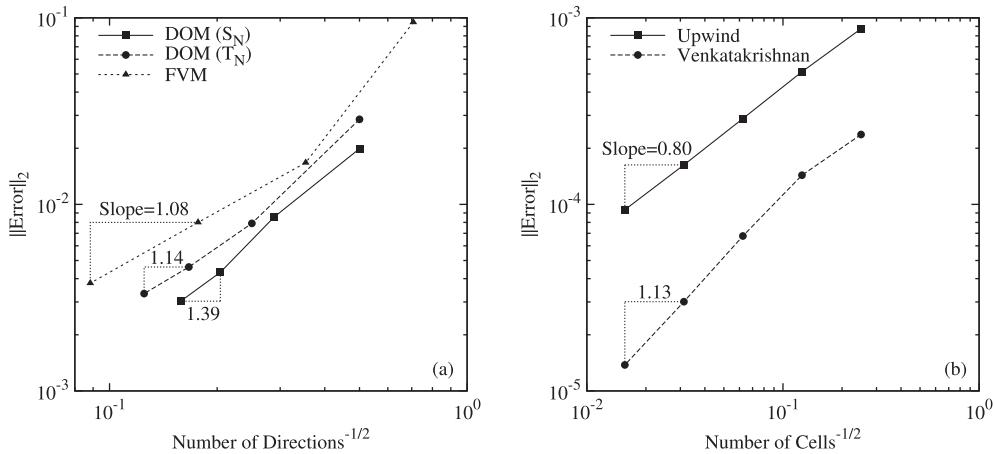


Fig. 6. Change in numerical error with (a) angular and (b) spatial discretization for the square enclosure.

DOM or FVM and varying levels of angular resolution. Quadrature rules used for the DOM include the  $S_2$ ,  $S_4$ ,  $S_6$ , and  $S_8$  schemes of Lathrop and Carlson [4] as well as the  $T_1$ ,  $T_2$ ,  $T_3$ , and  $T_4$  schemes of Thurgood et al. [5]. For the FVM, uniform angular meshes were employed over the hemisphere ( $0 \leq \theta \leq \pi/2$ ,  $0 \leq \psi \leq 2\pi$ ) with  $1 \times 2$ ,  $2 \times 4$ ,  $4 \times 8$ , and  $8 \times 16$  control angles in the polar and azimuthal directions, respectively. The figure confirms that reductions in error are achieved by increasing the angular resolution and that both DOM quadrature rules provide larger rates of decrease with number of directions than the FVM. The estimated slopes in regimes for asymptotic convergence are 1.39, 1.14, and 1.08 for the DOM with  $S_N$ , DOM with  $T_N$ , and FVM, respectively. It is interesting to note that the  $S_N$  scheme performs slightly better than the  $T_N$  scheme with consistently lower errors for the same number of propagation directions.

The accuracy of the spatial discretization was also assessed using a procedure similar to the one used for the angular discretization analysis. However, numerical solutions were compared to exact solutions for the DOM equations themselves instead of exact solutions of the RTE. These are spatially exact solutions to the angular approximation introduced by the DOM and therefore errors in the numerical solution are attributed to the spatial discretization only. Exact solutions for the DOM in rectangular enclosures were previously presented by Jessee et al. [83]. A unit square enclosure with cold and black walls that contains a hot, absorbing-emitting medium with  $\kappa = 0.01 \text{ m}^{-1}$  was modelled. Results for the effect of grid resolution on the error defined by Eq. (23) are presented in Fig. 6(b) for both the upwind and TVD spatial discretizations of the  $S_6$  DOM equations. The figure indicates that only first order-accuracy is achieved for both schemes as the slopes in the asymptotic regime are 0.80 and 1.13 for the upwind and TVD schemes, respectively. This first-order convergence observed by the TVD scheme is attributed to the large discontinuities that exist in the intensity of rays originating from the corners in all directions. Despite this lack of improvement in the order of accuracy over the upwind scheme as the mesh is refined, the TVD scheme still provides a far more accurate solution with fewer grid points. The absolute error obtained using the TVD scheme is nearly one order of magnitude lower than the first-order scheme.

### 3.3. Adaptive mesh refinement

#### 3.3.1. Square enclosure

The previous case for assessing the spatial discretization scheme was solved once again using the proposed AMR algorithm. The initial mesh consisted of 16 by 16 cells uniformly-spaced and divided into four equally-sized blocks. Using the DOM and the  $S_6$  quadrature scheme, solutions were obtained on subsequently refined meshes using various refinement criteria. Both the gradient of the direction-integrated intensity and the maximum gradient of the individual directional intensities were employed as a measure of the local truncation error. The two refinement criteria are defined by

$$\epsilon_1 \propto \nabla G \quad (25)$$

$$\epsilon_2 \propto \max(|\nabla I_1|, |\nabla I_2|, \dots, |\nabla I_M|) \quad (26)$$

where  $M$  is the total number of directions. Based on either of these criteria, the mesh is refined and blocks are added wherever the measures  $\epsilon_1$  or  $\epsilon_2$  are large.

The mesh statistics and resulting errors obtained using uniform refinement and AMR are tabulated in Table 1 and the effect of mesh resolution on grid convergence is plotted in Fig. 7(a). The convergence characteristics obtained using the maximum  $\nabla I_m$  criterion ( $\epsilon_2$ ) are almost identical to those obtained using uniform refinement. This is due to large discontinuities in the individual intensities that occur in all directions. The maximum gradient criterion flags all blocks for refinement and the resulting mesh is almost uniform. A slight degradation in convergence performance is observed when using the gradient of the direction-integrated intensity criterion ( $\epsilon_1$ ). This is explained by examining the solution contours for  $G/4\pi I_b$ , which are

**Table 1**  
AMR statistics for square enclosure test case.

Level	Uniform refinement		Refinement based on $\nabla G$			Refinement based on max $ \nabla I_m $		
	Cells	$\ \text{Error}\ _2$	Blocks	Cells	$\ \text{Error}\ _2$	Blocks	Cells	$\ \text{Error}\ _2$
0	16	2.4e-4	16	256	6.8e-5	16	256	6.8e-5
1	64	1.4e-4	52	832	4.4e-5	52	832	4.4e-5
2	256	6.8e-5	136	2176	4.0e-5	64	1024	3.0e-5
3	1024	3.0e-5	268	4288	2.1e-5	148	2368	2.5e-5
4	4096	1.4e-5	556	8896	1.9e-5	256	4096	1.4e-5
5			1444	23104	1.4e-5	520	8320	1.1e-5
6						1024	16384	6.5e-6

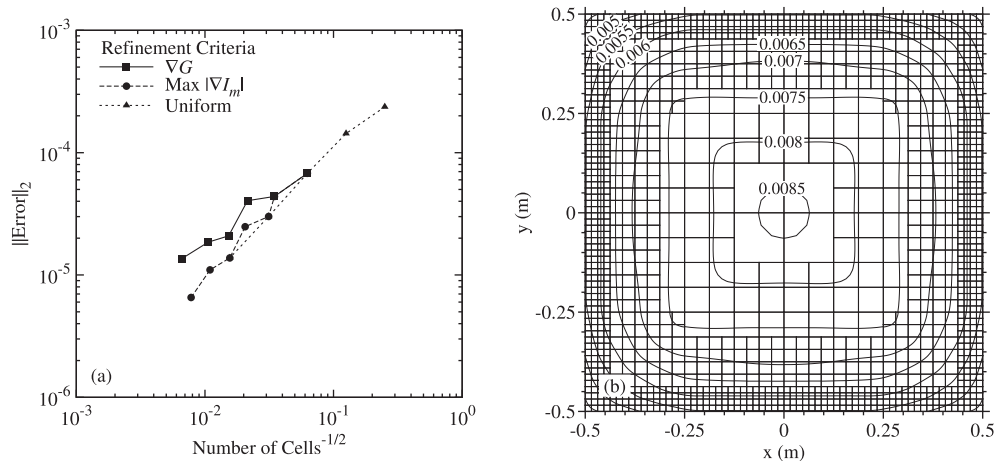


**Fig. 7.** Numerical solution for the square enclosure with cold and black walls containing a hot, absorbing-emitting medium with  $\kappa = 0.01 \text{ m}^{-1}$ . (a) Change in numerical error with mesh refinement; (b) computational mesh block boundaries and contours of normalized direction-integrated radiative intensity,  $G/(4\pi I_b)$ , after 5 levels of refinement using  $\nabla G$  refinement criterion (1444 blocks and 23 104 cells).

illustrated in Fig. 7(b) along with the block boundaries for the refined computational grid. These contours were obtained using the  $\epsilon_1$  criterion on the finest mesh. The direction-integrated intensity appears smooth when in fact large discontinuities in  $I_m$  are present. This results in only blocks near the wall being refined which do not help reduce the error along rays originating from the corners. Since the mesh is refined in incorrect locations when using the  $\epsilon_1$  criterion, the two-norm of the solution error decreases with decreasing average mesh spacing at a slower rate compared to using uniform refinement.

Due to the lack of disparate length scales in this particular test problem, AMR does not offer any significant improvements in terms of numerical efficiency over uniform refinement. Jessee et al. [83] obtained similar results for this test case when using a different AMR algorithm with similar physics-based refinement criterion. This emphasizes the need for refinement techniques that rely on improved estimates of the local error instead of physics-based criteria. More favourable results are expected for realistic test cases that do indeed contain a wider range of length scales.

### 3.3.2. Circular enclosure

To demonstrate the advantages of mesh refinement and the ability of the proposed multi-block body-fitted AMR method to deal with more complex geometry, the scheme was applied to an additional, more realistic test case which possessed both steep gradients and curved boundaries. The test case consisted of a discontinuous absorbing-emitting medium confined between two concentric circular enclosures, shown schematically in Fig. 8(a). Both walls are black with an emissivity of  $\epsilon_{w1} = \epsilon_{w2} = 1$ , inner wall temperature of  $T_{w1} = 100 \text{ K}$ , and outer wall temperature of  $T_{w2} = 0 \text{ K}$ . The walls are located at  $r_{w1} = 0.1 \text{ m}$  and  $r_{w2} = 2.0 \text{ m}$  while the medium inside the enclosure is discontinuous at  $r_3 = 0.59 \text{ m}$ . The temperature and absorption coefficient for the inner gas are  $T_{g1} = 100 \text{ K}$  and  $\kappa_{g1} = 10 \text{ m}^{-1}$  while they are  $T_{g2} = 0 \text{ K}$  and  $\kappa_{g2} = 100 \text{ m}^{-1}$  for the outer surrounding gas, respectively.

Radiative heat transfer between the two concentric cylinders was studied numerically by solving the RTE using the proposed Newton–Krylov–Schwarz (NKS) algorithm and the Venkatakrishnan TVD spatial discretization scheme. The FVM was used to discretize the angular coordinate and divide the hemisphere into 4 control angles in the polar- and 24 in the azimuthal-direction. The circular computational domain was sub-divided into an initial non-uniform, body-fitted mesh with two equally-sized blocks and 256 total cells. The maximum  $\nabla I_m$  AMR criterion ( $\epsilon_2$ ) was employed here as it provided the most favourable results in Section 3.3.1.

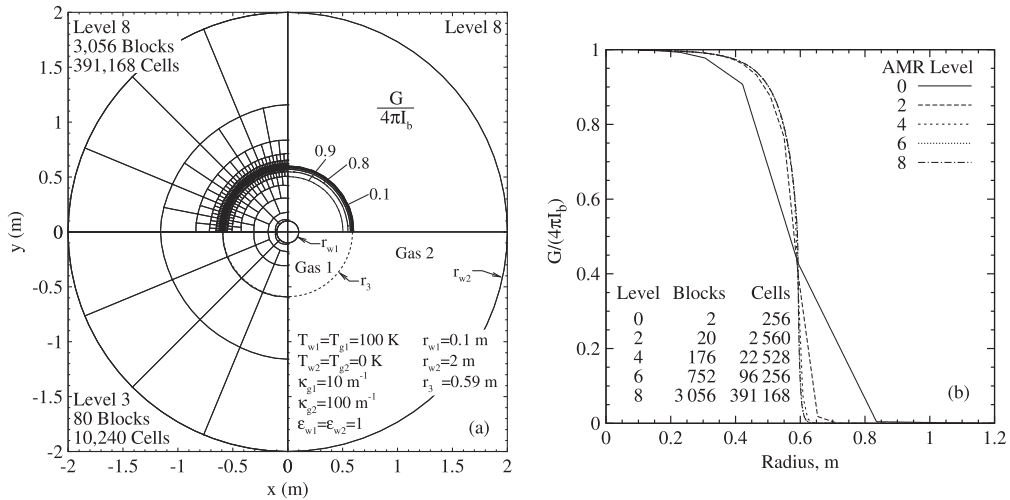


**Fig. 8.** Numerical solution for the circular enclosure with a discontinuous absorbing-emitting medium. (a) Problem description, computational mesh block boundaries, and contours of normalized direction-integrated radiative intensity after 8 levels of refinement; (b) direction-integrated intensity as a function of radius and AMR level.

Computed contours for  $G$  along with the mesh block boundaries after 8 levels of refinement are provided in Fig. 8(a). Block boundaries for an intermediate mesh refinement level, level 3, are also provided in the figure to illustrate the AMR process. The AMR algorithm correctly identified the large gradient in  $G$  at  $r = 0.59$  m produced by the discontinuity and refined the mesh in the corresponding location. A large improvement in the solution accuracy as the mesh is initially refined is observed in Fig. 8(b), which depicts the effect of mesh resolution on the radial profile for  $G$ . The figure also provides mesh statistics for each level including number of blocks and computational cells. Refining the mesh beyond six levels yielded little change in the solution. At the finest level, level 8, the mesh consists of 3056 blocks and 391 168 cells which corresponds to a refinement efficiency of 97.7% or an equivalent uniform mesh with 16 777 216 total cells.

### 3.4. Parallel performance

The parallel performance of the algorithm applied to the square enclosure case was assessed by examining both the strong and weak scaling properties. These two properties are a measure of the ability to demonstrate a proportionate increase in parallel speedup with more processors. For the strong scaling test, the problem size is held fixed while the number of processors used to perform the computation is varied. Weak scaling is measured by holding the work load per processor fixed and varying the problem size with the number of processors. These two scaling properties are measured by the parallel speedup  $S_p$  and efficiency  $\eta_p$  which are defined as

$$S_p = \frac{t_1}{t_p} \quad (27)$$

$$\eta_p = \frac{S_p}{p} \quad (28)$$

where  $t_1$  and  $t_p$  are the total wall times required to solve the problem with 1 and  $p$  processors, respectively.

#### 3.4.1. Strong scaling

Strong scaling was measured by dividing a uniform mesh of 512 by 512 cells amongst a number of equally sized blocks and solving the problem in parallel. The test was first carried out using two different meshes divided into a fixed number of blocks with either 32 by 32 or 64 by 64 cells. This allowed the work load per processor to be varied by changing the number of blocks assigned to each processor without affecting the partitioning of the mesh. As a result, only the effect of inter-processor communication on efficiency is observed since the number of residual evaluations to achieve converged solutions does not change. Each solution was said to have converged when the two-norm of the residual was reduced by 10 orders of magnitude from the original. Spatial discretization was performed using the Venkatakrishnan TVD scheme, angular discretization was performed with the  $S_6$  quadrature scheme, and ILU(0) was used as the block preconditioner. GMRES was restarted every 20 inner iterations and terminated after 80 iterations or when the residual for the linear problem was reduced by one order of magnitude. The resulting relationship between parallel speedup, efficiency, and number of processors is shown in Fig. 9(a) for the two meshes with different fixed block sizes. Excellent parallel performance is achieved with an efficiency greater than 85% on 256 processors. A slight deviation from ideal speedup begins to occur as the number of

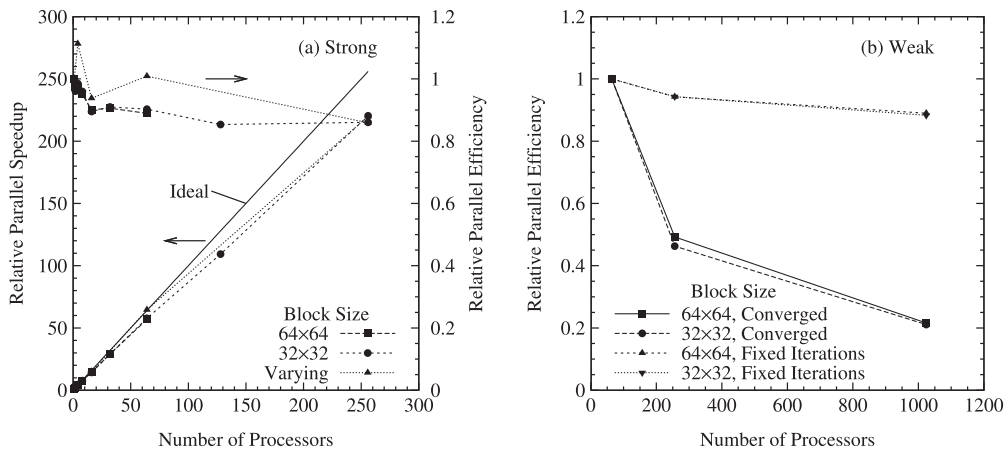


Fig. 9. Algorithm (a) strong and (b) weak scaling parallel performance.

processors is increased beyond 16 which is magnified as more processors are used. This degradation in parallel performance is attributed to the increase in the communication-to-work ratio for each processor as they are assigned less work and the amount of communication for each block remains the same. The observed effect of block size is minimal as almost no change in performance is observed when the block size is reduced by a factor of two from 64 by 64 cells to 32 by 32.

The strong scaling test was performed a third time with the same uniform mesh of 512 by 512 cells as the one used previously except the mesh partitioning was varied such that only one block was assigned to each processor. As a result, the mesh was divided into smaller blocks as more processors were used. This test not only measures the scalability of the particular implementation as the previous test did, but also the scalability of the overall algorithm. It includes the negative effect of partitioning on convergence which results from global Schwarz preconditioning in addition to the effect of communication. The results from this test are illustrated in Fig. 9(a) along with those obtained using the fixed block sizes. The results indicate similar performance to the fixed block size cases with a slight improvement observed when using fewer than 256 processors. This is due to the fact that the largest possible block sizes are used in the third case and the effect of the global preconditioner is minimized.

The effect of block size on the convergence characteristics of the Newton solver was assessed in more detail by plotting the convergence history against equivalent residual evaluations for the third strong scaling test, Fig. 10(a). The performance of the Newton method degrades as the block size is reduced and the total number of blocks increases. This is due to the reduced effectiveness of additive Schwarz preconditioning with increased partitioning. As a result, a slight increase in equivalent residual evaluations is observed every time the total number of blocks is increased. An unexpected decrease in the required number of residual evaluations is observed when the problem is solved using four processors (blocks) as compared to using no partitioning at all. A super-linear speedup is also observed in Fig. 9(a) between one and four processors. This super-linear speedup occurs as a result of the increasing accumulated cache size as processors are added on the IBM POWER6 platform.

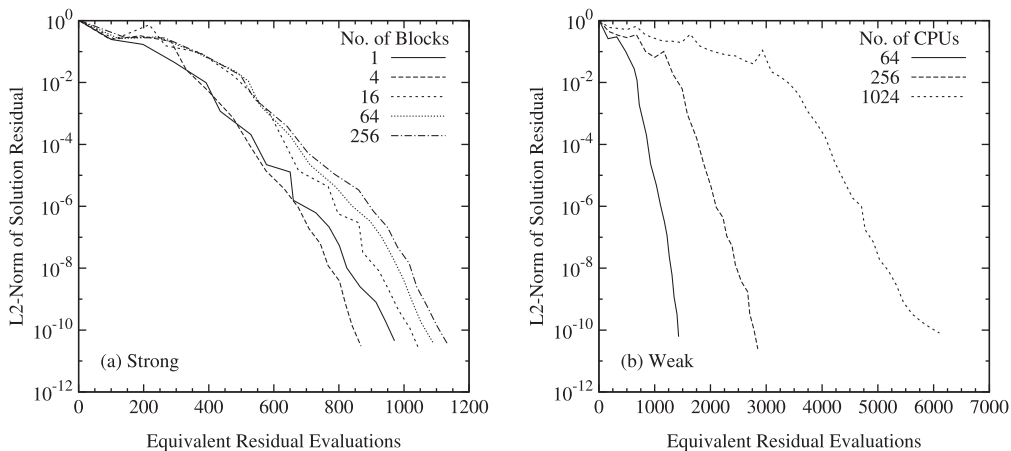


Fig. 10. Convergence histories for (a) strong scaling test using a varying block size and (b) weak scaling test with a fixed block size of 64 by 64 cells.

### 3.4.2. Weak scaling

Weak scaling performance of the proposed RTE solution algorithm is observed in Fig. 9(b) for two different block sizes of 32 by 32 and 64 by 64 cells. It was obtained by assigning each processor a single block and either iterating for a fixed number of Newton steps or until the solutions were fully converged. Solutions were deemed fully converged when the residual was reduced by ten orders of magnitude. Excellent performance for the fixed iteration case is observed up to 1024 processors (blocks) with a parallel efficiency greater than 90% relative to 64 processors. This indicates that the parallel implementation effectively minimizes the necessary inter-processor communication. However, efficiencies of only 50% and 20% were achieved on 256 and 1024 processors, respectively, when the solutions were fully converged. This drastic loss of performance is largely attributed to the effect of mesh partitioning and size on convergence history, which is illustrated in Fig. 10(b) for a block size of 64 by 64 cells. The number of residual evaluations increases drastically as the problem is discretized using a larger mesh with more blocks. For example, a factor of 16 increase in mesh size resulted in a four-fold increase in the number of residual evaluations to obtain a converged solution. This occurred since more GMRES iterations were required to solve the linear system (Eq. (20)) at each Newton iteration as the condition number of the Jacobian matrix,  $\mathbf{J}$ , increased significantly with problem size. This degradation of the GMRES performance is the main cause of the poor weak scaling obtained for the fully converged computations. It was less severe in the strong scaling test (Section 3.4.1) since the problem size remained fixed and was generally smaller than for the larger weak scaling cases. Only the partitioning was altered for the strong scaling test. Despite these weak scaling results, a substantial benefit is achieved through parallel solution of the radiation transport problem.

### 3.5. Serial performance

A final test was carried out to compare the serial performance of the proposed solver with other standard space-marching solution techniques discussed in this work. Two unit square enclosures were studied. The first enclosure was the same one studied in Section 3.2 containing a purely absorbing medium while the second enclosure contained a purely scattering medium. For the second enclosure, all walls are cold ( $T = 0$  K) and black except the bottom wall which is hot and black. The emissivity of all walls was set to one. The medium is also cold but scatters photons according to the high back-scattering B2 phase function described by Kim and Lee [84]. The effect of optical thickness, spatial discretization, and mesh resolution on overall performance for each solver is discussed for both test cases.

All of the solution methods considered in the serial performance assessment made use of the  $S_6$  DOM quadrature and solutions were obtained for three single-block mesh sizes: 32 by 32, 64 by 64, and 128 by 128 uniformly spaced cells. The proposed NKS scheme with a GMRES tolerance of 0.1 was used in combination with the upwind and Venkatakrishnan TVD discretizations. In addition to this, the standard space-marching solution technique outlined by Carlson and Lathrop [1] was employed with a variety of finite-volume schemes. Solutions were obtained using the space-marching technique with the upwind, central, CLAM, and the genuinely multi-dimensional (GM) [35] schemes. The high-resolution CLAM and GM schemes were implemented using the deferred correction procedure of Khosla and Rubin [85]. An explicit time-marching algorithm was also tested in this study for comparison purposes despite the poor performance characteristics of these types of solvers. The explicit solver makes use of FAS multigrid with a regular V-cycle and the five-stage optimally smoothing relaxation scheme of Van Leer et al. [86]. The iterations with the multigrid and Newton–Krylov solvers were stopped when residuals were reduced by 10 orders of magnitude while the space-marching solver used a convergence criterion of

$$\max(|\Delta I_m|) < 10^{-5} \quad (29)$$

where  $\max(|\Delta I_m|)$  is the maximum absolute change in spectral intensity between iterations. It should be noted that the tight convergence tolerances that are used for the time-stepping algorithms could not be met by the space-marching solver in most cases.

The resulting CPU times required to solve each case using the various methods are provided in Tables 2 and 3 for the purely absorbing and purely scattering media, respectively. For the absorbing case, the resulting upwind nature of the governing equations is easily handled by the space-marching technique. Both upwind and central schemes require only

**Table 2**  
CPU times(s) for square enclosure with absorbing-emitting medium.

Scheme	$\kappa = 0.01 \text{ m}^{-1}$			$\kappa = 10.0 \text{ m}^{-1}$		
	$32 \times 32$	$64 \times 64$	$128 \times 128$	$32 \times 32$	$64 \times 64$	$128 \times 128$
NKS (upwind)	1.6	11.2	78.1	1.0	5.8	38.2
NKS (limited)	1.9	12.8	90.7	2.5	8.4	52.1
Space-march (upwind)	0.0	0.1	0.5	0.0	0.1	0.5
Space-march (central)	0.0	0.1	0.5	0.0	0.1	0.5
Space-march (CLAM)	0.6	3.5	31.3	0.4	2.6	19.5
Space-march (GM)	0.3	1.7	14.5	0.3	1.5	11.4
FAS multigrid (upwind)	12.9	69.7	495.5	3.3	14.5	88.6
FAS multigrid (limited)	48.7	272.8	1612.2	25.4	58.3	313.5

**Table 3**  
CPU times(s) for square enclosure with scattering medium.

Scheme	$\sigma_s = 0.01 \text{ m}^{-1}$			$\sigma_s = 10.0 \text{ m}^{-1}$		
	$32 \times 32$	$64 \times 64$	$128 \times 128$	$32 \times 32$	$64 \times 64$	$128 \times 128$
NKS (upwind)	2.6	17.4	105.4	2.1	12.0	82.6
NKS (limited)	4.8	30.8	252.5	3.2	24.0	155.0
Space-march (upwind)	0.0	0.3	1.2	1.8	8.5	40.0
Space-march (central)	0.1	0.3	1.2	2.2	9.4	42.3
Space-march (CLAM)	0.7	6.0	52.5	6.6	47.2	439.2
Space-march (GM)	1.0	6.2	51.2	5.1	27.9	176.4
FAS multigrid (upwind)	14.7	79.0	516.5	19.8	71.7	334.8
FAS multigrid (limited)	55.8	301.1	1672.0	32.6	100.1	576.1

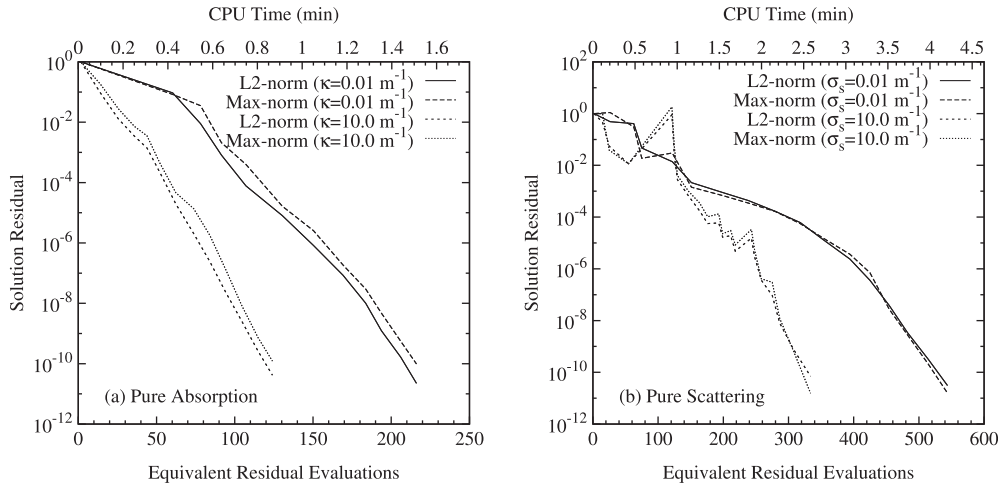


**Fig. 11.** Norms of solution residuals for square enclosure with (a) absorbing-emitting and (b) scattering media obtained using the proposed solution algorithm and the Venkatakrishnan TVD scheme on a mesh with 128 by 128 uniform cells.

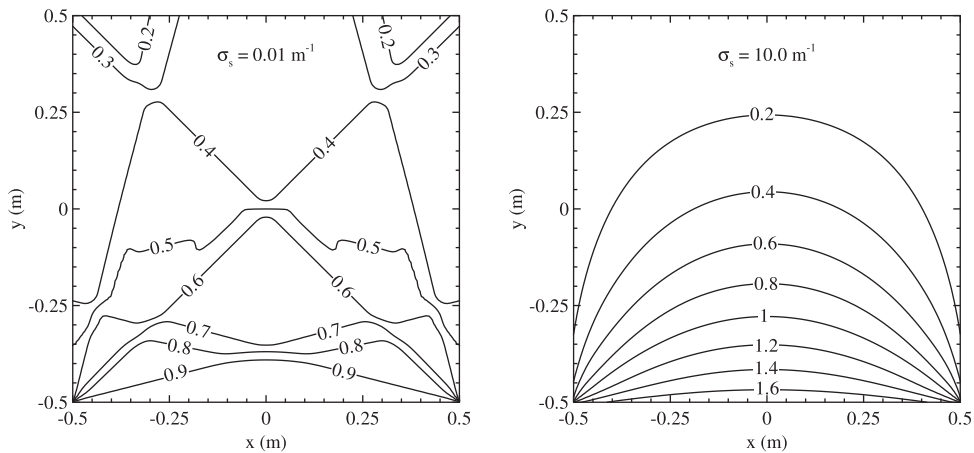


**Fig. 12.** Contours of normalized direction-integrated intensity,  $G/(2\pi I_b)$ , for square enclosure with scattering medium obtained using Venkatakrishnan TVD scheme on a mesh with 128 by 128 uniform cells.

one iteration in each direction to reduce the residual below the specified convergence criterion. Despite the added iterations required by the space-marching solver when using either of the two high-resolution schemes, they still outperform the proposed solution algorithm. The combined NKS and TVD scheme is a factor of 3.2 and 4.7 times slower on average than the CLAM scheme for the optically thin ( $\kappa = 0.01 \text{ m}^{-1}$ ) and thick ( $\kappa = 10 \text{ m}^{-1}$ ) cases, respectively. The GM scheme performs slightly better than the CLAM scheme. Multigrid performs the poorest, requiring excessively long solution times. The

solution time required for all schemes is observed to decrease with optical thickness. This is confirmed in Fig. 11(a) which shows the convergence histories for the implicit TVD scheme obtained on the finest mesh. As shown in the figure, the optically thick case converges much more rapidly.

The Newton–Krylov algorithm compared more favourably to the space-marching method when scattering was introduced. Comparing the high-resolution schemes, the Newton algorithm is at least twice as fast as the CLAM scheme and 1.3 times faster on average than the GM scheme for the optically thick case ( $\sigma_s = 10 \text{ m}^{-1}$ ). However, similar results to those obtained for the purely absorbing case are observed near the optically thin limit ( $\sigma_s = 0.01 \text{ m}^{-1}$ ). It is interesting to note that the convergence characteristics of both time-marching solvers improve as the optical thickness is increased while they decrease for the space-marching solvers. This loss of performance for the space-marching solver is due to the high back-scattering nature of the medium, which requires additional passes to propagate scattered rays in all directions. As the optical thickness increases, the coupling between intensities strengthens and is easily taken into account by the proposed scheme. Convergence histories are provided in Fig. 11(b) for the finest mesh. As for the purely absorbing case, convergence is much more rapid for large optical thickness ( $\sigma_s = 10.0 \text{ m}^{-1}$ ). For completeness, contours of the total radiative intensity are provided in Fig. 12. Increasing the optical thickness raises the total intensity near the hot wall as energy emitted from this wall is scattered back.

#### 4. Conclusion

A parallel implicit algorithm and TVD finite-volume scheme was successfully applied to the solution of the DOM and FVM discretizations of the RTE. The algorithm uses an implicit Newton–Krylov solution technique to handle non-linearities introduced by the discretization scheme and the strong omnidirectional coupling in scattering media. Block ILU( $p$ ) and additive Schwarz preconditioning were used to improve the effectiveness of the iterative linear solver. A somewhat unique AMR algorithm was also developed and applied to reduce the size of the computational mesh and the required computational resources while allowing the treatment of rather complex geometries without resorting to cut-cell or overlapping grid techniques. This AMR scheme is applicable to multi-block mesh consisting of anisotropic and/or stretched grid blocks with different levels of resolution and general quadrilateral cells. The overall performance of the algorithm was assessed by studying both purely absorbing and scattering media in various two-dimensional enclosures.

The proposed algorithm displayed excellent scaling characteristics with greater than 85% parallel efficiency up to 256 processors. Decreasing the block size had a small negative effect on convergence due to the additional partitioning used in the Schwarz preconditioner. However, the number of residual evaluations required to obtain a converged solution can increase significantly with problem size and condition number of the system. Comparing the CPU times required for several different solution techniques and high-resolution schemes, the proposed algorithm outperformed standard TVD space-marching methods by at least a factor of two for strongly scattering media. This favorable performance was not observed for weakly scattering and purely absorbing media. Nonetheless, the algorithm proves promising for large-scale computations of more realistic cases having complex geometry that must be solved in parallel. One of the main limitations of this algorithm is the large memory requirements well in excess of those for explicit or space-marching methods. Recommendations for future work include the implementation of low-memory iterative linear solvers, the use of more effective global preconditioners such as multi-level preconditioning methods [87–89], and the application of the algorithm to more realistic test cases. Additionally, error-based refinement criteria should be explored with specific application to test cases that include disparate scales.

#### Acknowledgements

The authors would like to thank Dr. Fengshan Liu from the National Research Council (NRC) for his advice and discussions on this research. Operational funds for this work have been provided by the Natural Sciences and Engineering Research Council (NSERC) and the Canadian Space Agency (CSA). Computational resources for performing all of the calculations reported herein were provided by the SciNet High Performance Computing Consortium at the University of Toronto and Compute/Calcul Canada through funding from the Canada Foundation for Innovation (CFI) and the Province of Ontario, Canada.

#### References

- [1] B.G. Carlson, K.D. Lathrop, Transport theory – the method of discrete ordinates, in: H. Greenspan, C.N. Kelber, D. Okrent (Eds.), *Computing Methods in Reactor Physics*, Gordon and Breach, London, 1968, pp. 171–266.
- [2] G.D. Raithby, E.H. Chui, A finite-volume method for predicting radiant heat transfer in enclosures with participating media, *J. Heat Transfer* 112 (2) (1990) 415–423.
- [3] J.C. Chai, H.S. Lee, S.V. Patankar, Finite volume method for radiation heat transfer, *J. Thermophys. Heat Transfer* 8 (3) (1994) 419–425.
- [4] K.D. Lathrop, B.G. Carlson, Discrete ordinates angular quadrature of the neutron transport equation, Report LA-3186, Los Alamos Scientific Laboratory, 1965.
- [5] C.P. Thurgood, A. Pollard, H.A. Becker, TN quadrature set for the discrete ordinates method, *J. Heat Transfer* 117 (4) (1995) 1068–1070.
- [6] W.A. Fiveland, Discrete ordinate methods for radiative heat transfer in isotropically and anisotropically scattering media, *J. Heat Transfer* 109 (3) (1987) 809–812.
- [7] J.S. Truelove, Discrete-ordinate solutions of the radiation transport equation, *J. Heat Transfer* 109 (4) (1987) 1048–1051.

- [8] G.D. Raithby, Evaluation of discretization errors in finite-volume radiant heat transfer predictions, *Numer. Heat Transfer B* 36 (3) (1999) 241–264.
- [9] J.C. Chai, H.S. Lee, S.V. Patankar, Ray effect and false scattering in the discrete ordinates method, *Numer. Heat Transfer B* 24 (4) (1993) 373–389.
- [10] F. Liu, H.A. Becker, A. Pollard, Spatial differencing schemes of the discrete-ordinates method, *Numer. Heat Transfer B* 30 (1) (1996) 23–43.
- [11] J.P. Jessee, W.A. Fiveland, Bounded, high-resolution differencing schemes applied to the discrete ordinates method, *J. Thermophys. Heat Transfer* 11 (4) (1997) 540–548.
- [12] P.H. Gaskell, A.K.C. Lau, Curvature-compensated convective transport: SMART a new boundedness-preserving transport algorithm, *Int. J. Numer. Methods Fluids* 8 (6) (1988) 617–641.
- [13] B. Van Leer, Towards the ultimate conservative difference scheme. V. A second-order sequel to Godunov's method, *J. Comput. Phys.* 32 (1979) 101–136.
- [14] B. Van Leer, Towards the ultimate conservative difference scheme. II. Monotonicity and conservation combined in a second order scheme, *J. Comput. Phys.* 14 (1974) 361–370.
- [15] A. Harten, High resolution schemes for hyperbolic conservation laws, *J. Comput. Phys.* 49 (1983) 357–393.
- [16] P.J. Coelho, Bounded skew high-order resolution schemes for the discrete ordinates method, *J. Comput. Phys.* 175 (2) (2002) 412–437.
- [17] M.L. Adams, E.W. Larsen, Fast iterative methods for discrete-ordinates particle transport calculations, *Prog. Nucl. Energ.* 40 (1) (2002) 3–159.
- [18] R.E. Alcouffe, Diffusion synthetic acceleration methods for the diamond-differenced discrete-ordinates equations, *Nucl. Sci. Eng.* 64 (2) (1977) 344–355.
- [19] J.S. Warsa, T.A. Wareing, J.E. Morel, Fully consistent diffusion synthetic acceleration of linear discontinuous SN transport discretizations on unstructured tetrahedral meshes, *Nucl. Sci. Eng.* 141 (3) (2002) 236–251.
- [20] J.S. Warsa, T.A. Wareing, J.E. Morel, Krylov iterative methods and the degraded effectiveness of diffusion synthetic acceleration for multidimensional SN calculations in problems with material discontinuities, *Nucl. Sci. Eng.* 147 (3) (2004) 218–248.
- [21] B. Guthrie, J.P. Holloway, B.W. Patton, GMRES as a multi-step transport sweep accelerator, *Transport Theor. Stat. Phys.* 28 (1) (1999) 83–102.
- [22] S.R. Mathur, J.Y. Murthy, Acceleration of anisotropic scattering computations using coupled ordinates method (COMET), *J. Heat Transfer* 123 (3) (2001) 607–612.
- [23] B. Chang, T. Manteuffel, S. McCormick, J. Ruge, B. Sheehan, Spatial multigrid for isotropic neutron transport, *SIAM J. Sci. Comput.* 29 (5) (2007) 1900–1917.
- [24] A. Fiterman, R. Ben-Zvi, A. Kribus, DOTS: pseudo-time-stepping solution of the discrete ordinate equations, *Numer. Heat Transfer B* 35 (2) (1999) 163–183.
- [25] N. Selçuk, G. Kirbaş, The method of lines solution of the discrete ordinates method for radiative heat transfer in enclosures, *Numer. Heat Transfer B* 37 (3) (2000) 379–392.
- [26] I. Ayranci, N. Selçuk, MOL solution of DOM for transient radiative transfer in 3-D scattering media, *J. Quant. Spectrosc. Radiat. Transfer* 84 (4) (2004) 409–422.
- [27] A.U. Bilge, T. Tarhan, N. Selçuk, Transient simulation of reacting radiating flows, *Int. J. Therm. Sci.* 45 (10) (2006) 969–976.
- [28] A.C. Hindmarsh, LSODE and LSODI, two new initial value ordinary differential equation solvers, *ACM-SIGNUM Newslett.* 15 (4) (1980) 10–11.
- [29] E. Fehlberg, Classical fourth- and lower order Runge–Kutta formulas with stepsize control and their application to heat transfer problems, *Computing* 6 (1–2) (1970) 61–71.
- [30] G.S. Jiang, C.W. Shu, Efficient implementation of weighted ENO schemes, *J. Comput. Phys.* 126 (1) (1996) 202–228.
- [31] D.S. Balsara, C.-W. Shu, Monotonicity preserving weighted essentially non-oscillatory schemes with increasingly high order of accuracy, *J. Comput. Phys.* 160 (2) (2000) 405–452.
- [32] R.G. McClarren, J.P. Holloway, T.A. Brunner, T.A. Mehlhorn, A quasilinear implicit Riemann solver for the time-dependent Pn equations, *Nucl. Sci. Eng.* 155 (2) (2007) 290–299.
- [33] R.G. McClarren, J.P. Holloway, A quasi-linear implementation of high-resolution time integration for the Pn equations, *Nucl. Sci. Eng.* 159 (3) (2008) 330–337.
- [34] M. Berger, M.J. Aftosmis, S.M. Murman, Analysis of slope limiters on irregular grids, in: 43rd AIAA Aerospace Sciences Meeting, Reno, NV, AIAA paper 2005-0490, 2005.
- [35] D. Balsara, Fast and accurate discrete ordinates methods for multidimensional radiative transfer – Part I. Basic methods, *J. Quant. Spectrosc. Radiat. Transfer* 69 (2001) 671–707.
- [36] P.L. Roe, Optimum upwind advection on a triangular mesh, ICASE report 90-75.
- [37] D. Sidilkover, P.L. Roe, Unification of some advection schemes in two dimensions, ICASE report 95-10.
- [38] A. Brandt, Guide to multigrid development, in: W. Hackbusch, U. Trottenberg (Eds.), *Multigrid Methods, Lecture Notes in Mathematics*, vol. 960, Springer, Berlin, 1982, pp. 220–312.
- [39] P.N. Brown, Y. Saad, Hybrid Krylov methods for nonlinear systems of equations, *SIAM J. Sci. Stat. Comput.* 11 (3) (1990) 450–481.
- [40] J.C. Chai, Transient radiative transfer in irregular two-dimensional geometries, *J. Quant. Spectrosc. Radiat. Transfer* 84 (2004) 281–294.
- [41] J. Gonçalves, P.J. Coelho, Parallelization of the discrete ordinates method, *Numer. Heat Transfer B* 32 (2) (1997) 151–173.
- [42] P.J. Coelho, J. Gonçalves, Parallelization of the finite volume method for radiation heat transfer, *Int. J. Numer. Methods Heat Fluid Flow* 9 (4) (1999) 388–404.
- [43] R.S. Baker, K.R. Koch, An Sn algorithm for the massively parallel CM-200 computer, *Nucl. Sci. Eng.* 128 (3) (1998) 312–320.
- [44] S.D. Pautz, An algorithm for parallel Sn sweeps on unstructured meshes, *Nucl. Sci. Eng.* 140 (2) (2002) 111–136.
- [45] R.S. Baker, A block adaptive mesh refinement algorithm for the neutral particle transport equation, *Nucl. Sci. Eng.* 141 (1) (2002) 1–12.
- [46] R.C. Ward, R.S. Baker, J.E. Morel, A diffusion synthetic acceleration method for block adaptive mesh refinement, *Nucl. Sci. Eng.* 152 (2) (2006) 164–179.
- [47] A. Dedner, P. Vollmler, An adaptive higher order method for solving the radiation transport equation on unstructured grids, *J. Comput. Phys.* 178 (2) (2002) 263–289.
- [48] J. Liu, H.M. Shang, Y.S. Chen, Parallel simulation of radiative heat transfer using an unstructured finite-volume method, *Numer. Heat Transfer B* 36 (1999) 115–137.
- [49] L.H. Howell, A parallel AMR implementation of the discrete ordinates method for radiation transport, in: T. Plewa, T. Linde, V.G. Weirs (Eds.), *Adaptive Mesh Refinement – Theory and Applications, Lecture Notes in Computational Science and Engineering*, vol. 41, Springer, Berlin, Heidelberg, 2005, pp. 255–270.
- [50] G. Krishnamoorthy, R. Rawat, P.J. Smith, Parallel computations of radiative heat transfer using the discrete ordinates method, *Numer. Heat Transfer B* 46 (2005) 19–38.
- [51] Ö. Yıldız, H. Bedir, A parallel solution to the radiative transport in three-dimensional participating media, *Numer. Heat Transfer B* 50 (1) (2006) 79–95.
- [52] J.S. Sachdev, C.P.T. Groth, J.J. Gottlieb, A parallel solution-adaptive scheme for multi-phase core flows in solid propellant rocket motors, *Int. J. Comput. Fluid Dyn.* 19 (2) (2005) 159–177.
- [53] J.S. Sachdev, C.P.T. Groth, A mesh adjustment scheme for embedded boundaries, *Commun. Comput. Phys.* 2 (6) (2007) 1095–1124.
- [54] C. Führer, G. Kanschat, A posteriori error control in radiative transfer, *Computing* 58 (4) (1997) 317–334.
- [55] J.I. Duo, Y.Y. Azmy, L.T. Zikatanov, A posteriori error estimator and AMR for discrete ordinates nodal transport methods, *Ann. Nucl. Energy* 36 (3) (2009) 268–273.
- [56] J.C. Ragusa, Y. Wang, A two-mesh adaptive mesh refinement technique for SN neutral-particle transport using a higher-order DGFEM, *J. Comput. Math.* 233 (12) (2010) 3178–3188.
- [57] Y. Wang, J.C. Ragusa, Standard and goal-oriented adaptive mesh refinement applied to radiation transport on 2D unstructured triangular meshes, *J. Comput. Phys.* 230 (3) (2011) 763–788.

- [58] C.P.T. Groth, S.A. Northrup, Parallel implicit adaptive mesh refinement scheme for body-fitted multi-block mesh, in: 17th AIAA Computational Fluid Dynamics Conference, Toronto, Ontario, Canada, AIAA paper 2005-5333, 2005.
- [59] Y. Saad, M.H. Schultz, GMRES: a generalized minimal residual algorithm for solving nonsymmetric linear systems, *SIAM J. Sci. Stat. Comput.* 7 (3) (1986) 856–869.
- [60] P. Cheng, Exact solutions for multi-dimensional radiative transfer in Cartesian coordinate configurations, Paper 1972-21, AIAA, 1972.
- [61] S.S. Dua, P. Cheng, Multi-dimensional radiative transfer in non-isothermal cylindrical media with non-isothermal bounding walls, *Int. J. Heat Mass Transfer* 18 (1975) 245–259.
- [62] R. Viskanta, M.P. Mengüç, Radiation heat transfer in combustion systems, *Prog. Energy Combust. Sci.* 13 (1987) 97–160.
- [63] S.K. Godunov, Finite-difference method for numerical computations of discontinuous solutions of the equations of fluid dynamics, *Mat. Sb.* 47 (1959) 271–306.
- [64] B. Engquist, S. Osher, One-sided difference approximations for nonlinear conservation laws, *Math. Comput.* 36 (1981) 321–352.
- [65] T.J. Barth, P.O. Fredrickson, Higher order solution of the Euler equations on unstructured grids using quadratic reconstruction, AIAA paper 90-0013, 1990.
- [66] V. Venkatakrishnan, Convergence to steady state solutions of the Euler equations on unstructured grids with limiters, *J. Comput. Phys.* 118 (1) (1995) 120–130.
- [67] Y. Saad, Krylov subspace methods on supercomputers, *SIAM J. Sci. Stat. Comput.* 10 (6) (1989) 1200–1232.
- [68] Y. Saad, *Iterative Methods for Sparse Linear Systems*, PWS Publishing Company, Boston, 1996.
- [69] R.S. Dembo, S.C. Eisenstat, T. Steihaug, Inexact Newton methods, *SIAM J. Numer. Anal.* 19 (2) (1982) 400–408.
- [70] X. Gao, C.P.T. Groth, Parallel adaptive mesh refinement scheme for three-dimensional turbulent non-premixed combustion, in: 46th AIAA Aerospace Sciences Meeting and Exhibit, Reno, Nevada, AIAA paper 2008-1017, 2008.
- [71] M.J. Berger, Adaptive mesh refinement for hyperbolic partial differential equations, *J. Comput. Phys.* 53 (1984) 484–512.
- [72] M.J. Berger, P. Colella, Local adaptive mesh refinement for shock hydrodynamics, *J. Comput. Phys.* 82 (1989) 67–84.
- [73] M.J. Berger, J.S. Saltzman, AMR on the CM-2, *Appl. Numer. Math.* 14 (1994) 239–253.
- [74] M.J. Aftomis, M.J. Berger, J.E. Melton, Robust and efficient cartesian mesh generation for component-base geometry, *AIAA J.* 36 (6) (1998) 952–960.
- [75] J.J. Quirk, An Adaptive Grid Algorithm for Computational Shock Hydrodynamics, Ph.D. Thesis, Cranfield Institute of Technology, 1991.
- [76] D. De Zeeuw, K.G. Powell, An adaptively refined cartesian mesh solver for the Euler equations, *J. Comput. Phys.* 104 (1993) 56–68.
- [77] J.J. Quirk, U.R. Hanebutte, A Parallel Adaptive Mesh Refinement Algorithm, ICASE report 93-63 .
- [78] W. Gropp, E. Lusk, A. Skjellum, *Using MPI*, MIT Press, Cambridge, MA, 1999.
- [79] P.J. Coelho, A comparison of spatial discretization schemes for differential solution methods of the radiative transfer equation, *J. Quant. Spectrosc. Radiat. Transfer* 109 (2) (2008) 189–200.
- [80] V. Venkatakrishnan, On the accuracy of limiters and convergence to steady state solutions, AIAA paper 93-0880.
- [81] T.J. Barth, D.C. Jespersen, The design and application of upwind schemes on unstructured meshes, AIAA paper 89-0366, 1989.
- [82] G.D. Van Albada, B. Van Leer, W.W. Roberts, A comparative study of computational methods in cosmic gas dynamics, *Astron. Astrophys.* 108 (1982) 76–84.
- [83] J.P. Jessee, W.A. Fiveland, L.H. Howell, P. Colella, R.B. Pember, An adaptive mesh refinement algorithm for the radiative transport equation, *J. Comput. Phys.* 139 (2) (1998) 380–398.
- [84] T.K. Kim, H. Lee, Effect of anisotropic scattering on radiative heat transfer in two-dimensional rectangular enclosures, *Int. J. Heat Mass Transfer* 31 (8) (1988) 1711–1721.
- [85] P.K. Khosla, S.G. Rubin, A diagonally dominant second-order accurate implicit scheme, *Comput. Fluids* 2 (2) (1974) 207–209.
- [86] B. Van Leer, C. Tai, K.G. Powell, Design of optimally smoothing multi-stage schemes for the Euler equations, AIAA paper 89-1933.
- [87] X.-C. Cai, W.D. Gropp, D.E. Keyes, R.G. Melvin, D.P. Young, Parallel Newton–Krylov–Schwarz algorithms for the transonic full potential equations, *SIAM J. Sci. Comput.* 19 (1) (1998) 246–265.
- [88] K. Geraschewski, A. Bhattacharjee, R. Grauer, D. Keyes, B. Smith, Using Krylov–Schwarz methods in an adaptive mesh refinement environment, in: T. Plewa, T. Linde, V. Gregory Weirs (Eds.), *Adaptive Mesh Refinement – Theory and Applications*, Lecture Notes in Computational Science and Engineering, vol. 41, Springer, Berlin, Heidelberg, 2005, pp. 115–124.
- [89] E.E. Prudencio, X.-C. Cai, Parallel multilevel restricted Schwarz preconditioners with pollution removing for PDE-constrained optimization, *SIAM J. Sci. Comput.* 29 (3) (2007) 964–985.